Particulate Photocatalyst Sheets Based on Carbon Conductor Layer for Efficient Z-Scheme Pure-Water Splitting at Ambient Pressure

Qian Wang,[†,‡] Takashi Hisatomi,[†,‡] Yohichi Suzuki,[§] Zhenhua Pan,[†] Jeongsuk Seo,[†,‡] Masao Katayama,[†,‡] Tsutomu Minegishi,[†,‡] Hiroshi Nishiyama,[†,‡] Tsuyoshi Takata,[†,‡] Kazuhiko Seki,[§] Akihiko Kudo,[∥] Taro Yamada,[†,‡] and Kazunari Domen*,[†,‡]

[†]Department of Chemical System Engineering, School of Engineering, The University of Tokyo, 7-3-1 Hongo, Bunkyo-ku, Tokyo 113-8656, Japan

[‡]Japan Technological Research Association of Artificial Photosynthetic Chemical Process (ARPChem), 2-11-9 Iwamotocho, Chiyoda-ku, Tokyo 101-0032, Japan

[§]National Institute of Advanced Industrial Science and Technology (AIST), 1-1-1 Higashi, Tsukuba, Ibaraki 305-8565, Japan

[∥]Department of Applied Chemistry, Tokyo University of Science, 1-3 Kagurazaka, Shinjuku-ku, Tokyo 162-8601, Japan

S *Supporting Information*

ABSTRACT: Development of sunlight-driven water splitting systems with high efficiency, scalability, and cost-competitiveness is a central issue for mass production of solar hydrogen as a renewable and storable energy carrier. Photocatalyst sheets comprising a particulate hydrogen evolution photocatalyst (HEP) and an oxygen evolution photocatalyst (OEP) embedded in a conductive thin film can realize efficient and scalable solar hydrogen production using Z-scheme water splitting. However, the use of expensive precious metal thin films that

SrTiO$_3$:La,Rh/C/BiVO$_4$:Mo sheet

also promote reverse reactions is a major obstacle to developing a cost-effective process at ambient pressure. In this study, we present a standalone particulate photocatalyst sheet based on an earth-abundant, relatively inert, and conductive carbon film for efficient Z-scheme water splitting at ambient pressure. A SrTiO$_3$:La,Rh/C/BiVO$_4$:Mo sheet is shown to achieve unassisted pure-water (pH 6.8) splitting with a solar-to-hydrogen energy conversion efficiency (STH) of 1.2% at 331 K and 10 kPa, while retaining 80% of this efficiency at 91 kPa. The STH value of 1.0% is the highest among Z-scheme pure water splitting operating at ambient pressure. The working mechanism of the photocatalyst sheet is discussed on the basis of band diagram simulation. In addition, the photocatalyst sheet split pure water more efficiently than conventional powder suspension systems and photoelectrochemical parallel cells because H$^+$ and OH$^-$ concentration overpotentials and an *IR* drop between the HEP and OEP were effectively suppressed. The proposed carbon-based photocatalyst sheet, which can be used at ambient pressure, is an important alternative to (photo)electrochemical systems for practical solar hydrogen production.
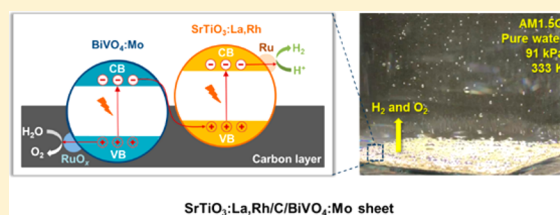
■ INTRODUCTION

From the viewpoint of mitigating environmental and energy issues caused by mass consumption of exhaustible fossil fuels, the need for alternative renewable and economically viable energy sources is widely recognized.[1] One attractive approach is to apply solar energy to split water into hydrogen and oxygen, and to use the hydrogen as a storable, sustainable energy carrier on a scale commensurate with global demand.[2−4] Photocatalytic and photoelectrochemical (PEC) systems offer a straightforward route to solar hydrogen production.[5,6] Intense effort has been focused on development of standalone PEC cells based on photoelectrodes integrated with silicon,[7] and dye-sensitized[8] and perovskite solar cells.[9] The solar-to-hydrogen energy conversion efficiency (STH) of such PEC systems has reached 12.4%.[10] However, large-scale PEC application is still challenging due to high fabrication costs, insufficient stability and the complexity of the devices.[11−13] At present, technologies involving photovoltaics are too expensive to produce hydrogen at a levelized cost comparable to that of

fossil-fuel derived electricity.[5,14] Direct decomposition of water into hydrogen and oxygen via particulate semiconductor photocatalysts is a promising alternative approach because of its simplicity and low cost. However, the STH of photocatalytic water-splitting systems is still 1 order of magnitude lower than that of state-of-the-art systems based on PEC and photovoltaic-powered water splitting.[5,15]

Z-scheme photocatalytic systems using two-step photo-excitation of a hydrogen evolution photocatalyst (HEP) and an oxygen evolution photocatalyst (OEP) are suitable for harvesting solar energy. They have been the subject of considerable attention because narrow band gap semiconductors with either a water reduction or oxidation potential can be employed to split water using solar energy.[16−18] For Z-scheme systems to operate effectively, it is important to realize efficient electron transfer from the OEP to the HEP, and to suppress
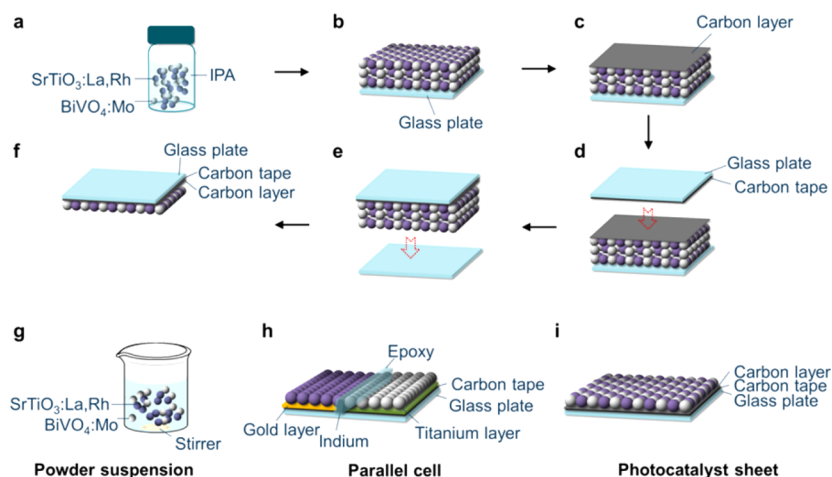
Figure 1. (a−f) Schematic illustration of the preparation procedure for a SrTiO$_3$:La,Rh/C/BiVO$_4$:Mo sheet by particle transfer. (a) Suspending a mixture of HEP and OEP powders in IPA, (b) drop-casting the mixture on a glass plate, (c) depositing a carbon layer by sputtering, (d) bonding to another glass plate, (e) lifting off the primary glass plate, and (f) ultrasonication. Schematic diagrams of (g) powder suspension consisting of SrTiO$_3$:La,Rh and BiVO$_4$:Mo, (h) parallel cell with side-by-side placement of SrTiO$_3$:La,Rh/Au and BiVO$_4$:Mo/Ti electrodes, and (i) SrTiO$_3$:La,Rh/C/BiVO$_4$:Mo photocatalyst sheet for Z-scheme water-splitting.

reverse reactions. To this end, we have designed and developed photocatalyst sheets that consist of HEP and OEP particles embedded in a conducting medium for effective electron transfer.[19] It was found that La- and Rh-codoped SrTiO$_3$ (SrTiO$_3$:La,Rh) and Mo-doped BiVO$_4$ (BiVO$_4$:Mo) powders anchored in a Au layer (SrTiO$_3$:La,Rh/Au/BiVO$_4$:Mo) achieved the highest STH of 1.1% for Z-scheme pure-water splitting without the need for supporting electrolytes, buffering reagents, redox couples, an applied voltage, or circulation of the reaction solution.[19] This photocatalyst sheet is ten times more active than the most active particle suspension system using similar photocatalysts,[20] and represents a new approach to scalable and efficient solar water splitting. However, the use of costly gold as the conducting material, together with the drastic decrease in water-splitting activity due to reverse reactions as the background pressure increases, are major obstacles to large-area implementation of the photocatalyst sheet system for solar hydrogen production.

Our previous study has shown that Au and Rh that have high chemical stability and relatively large work functions are suitable as a conductive layer of the photocatalyst sheet.[21] The work function of carbon is reportedly 5.0 eV,[22,23] which is close to those of Au (5.1 eV) and Rh (5.0 eV).[23] In addition, carbon is less active than gold for oxygen reduction reaction (ORR), which is a typical backward reaction competing with the water splitting reaction,[24,25] and normally used as a conductive support for ORR catalysts.[26] Therefore, it is expected that carbon is well suited for application as a conduction layer in the photocatalyst sheet. In the present paper, we describe a photocatalyst sheet that uses an earth-abundant and conducting carbon film for electron transfer, with the structure SrTiO$_3$:La,Rh/C/BiVO$_4$:Mo. Such sheets were found to exhibit a high STH of 1.0% for Z-scheme pure-water splitting at ambient pressure.

■ EXPERIMENTAL SECTION

Preparation of SrTiO$_3$:La,Rh/C/BiVO$_4$:Mo Photocatalyst Sheets. SrTiO$_3$:La,Rh (La/(La + Sr) = Rh/(Rh + Ti) = 4 mol %) and BiVO$_4$:Mo (Mo/V = 0.05 mol %) were synthesized via a two-step solid state reaction[27] and aqueous processes,[28] respectively, according to previously reported procedures. SrTiO$_3$:La,Rh/C/BiVO$_4$:Mo

photocatalyst sheets were fabricated by the particle transfer method (Figure 1a–f).[29] In the initial step, a mixture of SrTiO$_3$:La,Rh and BiVO$_4$:Mo powders (10 mg each) was dispersed in 0.5 mL of isopropanol (Wako Pure Chemical, 99.9%) by sonication for about 30 min. The powder ink was then drop-cast on a glass substrate (56 µL cm^{-2}). After drying at room temperature, a thin carbon layer (ca. 1 µm thick) was deposited by direct current (DC) magnetron sputtering (ES-250L, Eiko Engineering, Co., Ltd.) in an Ar atmosphere with a background pressure of 0.5 Pa for 4.5 h at 75 W and room temperature unless otherwise noted. The resulting carbon film holding the particulate photocatalysts was firmly attached to a second glass plate using adhesive carbon tape, and then lifted off the primary glass plate. Finally, the photocatalyst sheet was ultrasonicated twice, for 2 min each time, in distilled water in order to remove excess particles that had piled up on the particle layer. A schematic illustration and pictures of SrTiO$_3$:La,Rh/Au/BiVO$_4$:Mo photocatalyst sheets (3 × 3 and 5 × 5 cm^2) are presented in Figure 1i and Figure S1 in the Supporting Information. For comparison, SrTiO$_3$:La,Rh/Au/BiVO$_4$:Mo photocatalyst sheets,[19] suspension of the photocatalyst powders (Figure 1g) and parallel cells of SrTiO$_3$:La,Rh/Au and BiVO$_4$:Mo/Ti electrodes (Figure 1h) were also prepared. The details of preparation of the parallel cell are presented in the Supporting Information.

Overall Water-Splitting Reaction. Prior to the overall water-splitting reaction, the photocatalyst sheet samples were modified with nanoparticulate Ru species and Cr$_2$O$_3$ shell by photodeposition.[19] The detailed procedures are presented in the Supporting Information. Z-scheme water-splitting reactions were performed in the same closed gas circulation system with top irradiation by a 300 W Xe lamp equipped with a cutoff filter (λ > 420 nm) or a solar simulator (Asahi Spectra Co., Ltd., HAL-320). The photocatalyst sheet samples (ca. 7.5 cm^2) were placed at the bottom of the reaction cell containing the reactant (40 mL). The reactant was pure water, and no sacrificial reagent, redox couple, electrolyte, or pH adjustment was used unless otherwise noted. The reaction temperature and the background pressure were 288 K and 5 kPa, respectively, unless otherwise noted. The temperature of the reactant solution was raised by a water bath when necessary.

For powder suspension systems, a mixture of SrTiO$_3$:La,Rh and BiVO$_4$:Mo powders with an optimum amount of 10 mg each[21] was dispersed in 40 mL of distilled water. Photodeposition of Ru (0.4 µmol) was conducted in the manner described above. The pH of the solution was adjusted to 3.5 using H$_2$SO$_4$ (aq.) when necessary. The effect of a redox mediator was investigated in an aqueous solution of FeCl$_3$ (2 mM), the pH of which was adjusted to 2.4 using H$_2$SO$_4$, as reported previously.[30]

An aqueous solution of $RuCl_3 \cdot 3H_2O$ without pH adjustment was used for photodeposition of Ru ($0.02\ \mu mol\ cm^{-2}$) on a PEC parallel cell. The water-splitting activity of the PEC parallel cell was examined in an aqueous solution of H_2SO_4 (pH 3.5), 0.1 M Na_2SO_4 (pH 6.8) or 0.1 M potassium phosphate buffer (pH 6.8). H_2SO_4 (aq.) or NaOH (aq.) was added for pH adjustment of the Na_2SO_4 solution, while H_3PO_4 (aq.) or KOH (aq.) was used for the potassium phosphate buffer solution when necessary.

Quantum Yield Measurement. The apparent quantum yield (AQY) for Z-scheme water splitting involving two-step photo-excitation can be calculated using the following equation:

$$AQY(\%) = [4 \times n(H_2)]/n(\text{photons}) \times 100$$

where $n(H_2)$ and $n(\text{photons})$ indicate the number of produced H_2 molecules and the number of incident photons, respectively. Hydrogen and oxygen were evolved under illumination by a 300 W Xe lamp with a band-pass filter with a central wavelength of 418.6 nm and a full width at half-maximum of 9.5 nm.

STH Measurement. The water-splitting reaction was performed under simulated sunlight irradiation. The STH is given by

$$STH(\%) = (R(H_2) \times \Delta G_r)/(P \times S) \times 100$$

where $R(H_2)$, ΔG_r, P, and S denote the rate of hydrogen evolution during the water-splitting reaction, the *Gibbs energy* for the reaction (H_2O (l) → H_2 (g) + 1/2 O_2 (g)), the energy intensity of the AM1.5G solar irradiation (100 mW cm^{-2}), and the irradiated sample area (ca. 7.5 cm^2), respectively. The values of ΔG_r used for the calculation were 226 kJ mol^{-1} at 288 K and 5 kPa, 220 kJ mol^{-1} at 331 K and 10 kPa, and 229 kJ mol^{-1} at 331 K and 91 kPa.[19]

Characterization. Scanning electron microscopy and energy dispersive X-ray fluorescence spectroscopy (SEM-EDX) images were obtained using Hitachi SU8020 and Horiba EX-370 systems. X-ray photoelectron spectroscopy (XPS) measurements were performed using a monochromatic Mg Kα source ($h\nu$ = 1253.6 eV) excited at 8 kV and 10 mA. The analysis chamber pressure was on the order of 10^{-6} Pa. The binding energies were corrected using the Au $4f_{7/2}$ peak (84.0 eV) for a Au layer that was deposited as a reference. To perform XPS measurements of as-fabricated samples, the composite particulate photocatalyst layer and deposited carbon film was fully transferred from the glass plate to an indium plate without the use of carbon tape. This was done in order to avoid any signals from the carbon tape used for particle transfer. Likewise, for cross-sectional SEM-EDX measurements and XPS analysis of samples that had undergone a water-splitting reaction, a gold layer with a thickness of greater than 3 μm was deposited beneath the carbon layer. To determine the work function of the deposited materials, photoelectron spectroscopy in air (PESA) was carried out using a surface analyzer (Riken-Keiki Co., Ltd., AC-3). X-ray diffraction (XRD) patterns were obtained using a Rigaku Ultima III using Cu Kα radiation at 40 kV and 40 mA. Visible Raman spectra were collected using a NRS-7100 Raman spectrometer (JASCO) with excitation by a green laser line at 532 nm. The spectra were deconvoluted into two Gaussian components in the D-band and G-band, centered at around 1350 and 1580 cm^{-1}, respectively. The electrical conductivity was measured using a resistivity measuring system (Mitsubishi Chemical Analytech Co., Ltd., MCP-T610).

Electrochemical ORR Activity Measurements. Carbon and gold were deposited on titanium plates ($1 \times 1\ cm^2$) by DC sputtering and vacuum evaporation, respectively. The thickness of the carbon and gold layers were 1 μm and 350 nm, respectively, the same as those used in the preparation of $SrTiO_3$:La,Rh/C/$BiVO_4$:Mo and $SrTiO_3$:La,Rh/Au/$BiVO_4$:Mo photocatalyst sheets,[19] respectively, and the same deposition conditions were also used. Electrical contact was established by embedding a copper wire in indium at the bottom of the sample. The copper wire and indium was encapsulated with epoxy. The exposed area of the electrode after packaging was 0.3 cm^2.

Electrochemical measurements for evaluating the ORR activity were performed in a three-electrode system with a Ag/AgCl reference and carbon counter electrodes. Linear sweep voltammograms for the ORR were acquired in a 0.1 M Na_2SO_4 aqueous solution (pH 6.7) at 298 K

while purging with Ar or O_2 gas at atmospheric pressure. The potential was swept from 1.23 to 0.20 V vs RHE at a scan rate of 10 mV s^{-1}.

Band Diagram Calculation. Band diagrams and carrier density distributions of the photocatalyst sheet were calculated using a semiconductor device simulator (AFORS-HET).[31] The semiconductor equations involving generation, migration, and recombination of charge carriers were solved self-consistently. The electrolyte was regarded as a hypothetical metal with a work function 5.055 eV, located at the middle of the hydrogen evolution and oxygen evolution potentials. The work function of DC-sputtered carbon and silver are 5.2 and 4.3 eV, respectively. Semiconducting properties of particulate $SrTiO_3$:La,Rh and $BiVO_4$:Mo photocatalysts are not readily available and thereby assumed from relevant material and physical parameters.[7,21,28,32−40] The material parameters used are presented in Table S1 and S2 in the Supporting Information. The impurity level of $SrTiO_3$:La,Rh, located at 2.3 eV below the conduction band, was regarded as the effective valence band.[32] The number density of Rh (4 mol % to Ti) was regarded as the density of states of the impurity level. The hole mobility in the impurity level is unknown but is expected to be smaller than that of the electron mobility in the conduction band. Accordingly, the hole mobility was assumed to be approximately 1000th of the electron mobility. In $BiVO_4$:Mo, the hole mobility was assumed to be the same with the electron mobility.

In the nonequilibrium calculation under AM1.5 illumination, the incident light enters from the electrolyte sides and charge carriers are generated following the Lambert−Beer law. The absorption coefficient of ZnO, which was implemented in AFORES-HET, was adopted as those of $SrTiO_3$:La,Rh and $BiVO_4$:Mo. Direct electron−hole recombination was considered in both $SrTiO_3$:La,Rh and $BiVO_4$:Mo. The recombination rate constant k_r was chosen so that the carrier lifetime $\tau = 1/(k_r \times \text{majority carrier concentration})$ became equal to 10 ns. Oxygen evolution on $SrTiO_3$:La,Rh and hydrogen evolution on $BiVO_4$:Mo were not considered. The total current density j_{tot} is the sum of the current densities induced by electron and hole migration, i.e., $j_{tot} = j_e + j_h$, where j_e and j_h are the current densities of electrons and holes, respectively. The total current density of 3.7×10^{-1} mA cm^{-2} was assumed from the hydrogen evolution rate of 6.9 $\mu mol\ h^{-1}$ cm^{-2} for $SrTiO_3$:La,Rh/C/$BiVO_4$:Mo.

■ RESULTS AND DISCUSSION

Characterization of Carbon Species in $SrTiO_3$:La,Rh/C/$BiVO_4$:Mo Sheets. The morphology of the $SrTiO_3$:La,Rh/C/$BiVO_4$:Mo photocatalyst sheets was observed by SEM-EDX. The images in Figure S2 in the Supporting Information show a carbon layer with a thickness of ca. 1 μm supporting a thin particle layer consisting of both $SrTiO_3$:La,Rh and $BiVO_4$:Mo photocatalysts. This structure, similar to that of the $SrTiO_3$:La,Rh/C/$BiVO_4$:Mo photocatalyst sheets, is essential in order to avoid the electrical resistance associated with grain boundaries, and to allow efficient transfer of electrons between the HEP and OEP particles.

The electrical conductivity of the carbon film was measured to be 2.6×10^4 S m^{-1} at room temperature. Figure 2a and 2b shows the results of C 1s XPS and visible Raman spectroscopy, respectively, for the deposited carbon film. The C 1s spectrum can be deconvoluted into three mixed Lorentzian−Gaussian peaks, which are attributed to sp^2 and sp^3 hybridized C−C or C−H bands, and C=O bonds.[41] The ratios and binding energies for carbon species in $SrTiO_3$:La,Rh/C/$BiVO_4$:Mo photocatalyst sheets are presented in Table S3 in the Supporting Information. The sp^2 hybridized bonds, which have a high electrical conductivity,[42] were dominant (78%) in the carbon layer. The sputtered carbon films were further investigated using visible Raman spectroscopy because of the high sensitivity of this technique for analyzing sp^2-hybridized carbon atoms, due to excitation of their π state.[43] Ideal graphite
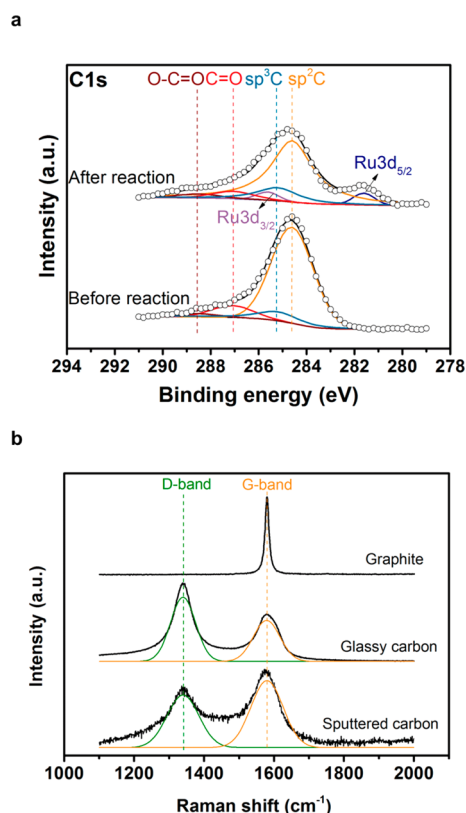
a

b

Figure 2. (a) C 1s core level XPS spectra of $SrTiO_3$:La,Rh/C/$BiVO_4$:Mo photocatalyst sheets before and after the water-splitting reaction. (b) Visible Raman spectra of deposited carbon layer, graphite and glassy carbon.

exhibits a single G-band peak at 1580 cm^{-1} related to the in-plane bond stretching motion of pairs of sp^2 carbon atoms.[44,45] However, similar to that for glassy carbon, the spectra of sputter carbon exhibited strong D- and G-bands, which indicated the amorphous nature of the films.[43,44] The D-band to G-band intensity ratio (I_D/I_G) of 1.1 and the broadness of the G band indicate the presence of small graphitic clusters.[41,45] These observations suggest that the sputtered carbon film consists of mainly sp^2 species in puckered ring-like configurations, with few sp^3 species.[44] As shown in the XRD pattern in Figure S3 in the Supporting Information, a very weak peak appears at $2\theta = 26.5°$ with a full-width at half-maximum of 0.15°, and could be assigned to diffraction from (002) graphite planes. This is evidence for the low degree of graphitization of the material. All these observations indicate that the sputtered carbon layer is partially graphitic and thus conductive. Its work function was determined to be 5.2 eV using PESA, as shown in Figure S4 in the Supporting Information, which is similar to that for glassy carbon, and larger than the typical values for Au and graphite. The relatively large work function for the sputtered carbon is due to $\sigma-\pi$ hybridization, which leads to deeper HOMO levels.[22]

Photocatalytic Activity of $SrTiO_3$:La,Rh/C/$BiVO_4$:Mo Sheets. The $SrTiO_3$:La,Rh/C/$BiVO_4$:Mo photocatalyst sheet splits water under visible light ($\lambda > 420$ nm) irradiation. A typical time course is shown in Figure 3. Hydrogen and oxygen were steadily evolved at a stoichiometric ratio over a period of 17 h. The results of an XPS analysis indicated that the carbon layer did not undergo obvious degradation during the water-splitting reaction (Figure 2a and Table S3). The water-splitting
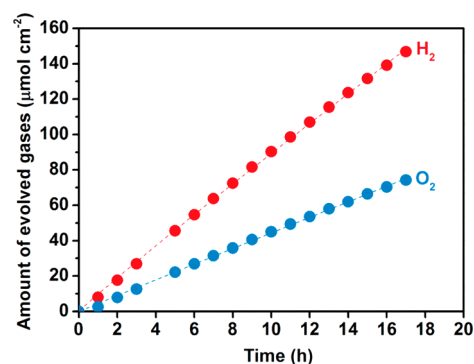

Figure 3. Time course for overall water splitting on Ru-modified $SrTiO_3$:La,Rh/C/$BiVO_4$:Mo sheet under Xe lamp (300 W) illumination ($\lambda > 420$ nm). The reaction was carried out at 288 K and 5 kPa.

activity of the photocatalyst sheet was about 20 times higher than that of a similar sheet without any conductive layer (Figure S5 in the Supporting Information). Clearly, H_2 and O_2 were produced by two-step photoexcitation of the $SrTiO_3$:La,Rh and $BiVO_4$:Mo photocatalysts, and charge transfer through the carbon layer. The STH of the photocatalyst sheet for overall water splitting was calculated to be 0.3% on the basis of the average rate of hydrogen evolution over a 6-h reaction at a temperature of 288 K and a pressure of 5 kPa under simulated sunlight irradiation (Figure S6 in the Supporting Information). The photocatalytic activity of the $SrTiO_3$:La,Rh/C/$BiVO_4$:Mo sheet for overall pure water splitting was further improved by heating the substrate during the carbon-sputtering process because of reduction in the contact resistance between the semiconductor particles and the carbon film[19] (Figure S7 in the Supporting Information). The sheet sample with a carbon deposition temperature of 373 K exhibited a 40% higher water-splitting rate than the sample with a carbon film deposited at room temperature.

The water-splitting activity of the carbon-based photocatalyst sheet was close to and much higher than those of gold-based[19] and silver-based[21] photocatalyst sheets, respectively. To understand the influence of the conductor materials on the behavior of photogenerated carriers, band diagrams and carrier density distributions of photocatalyst sheets were analyzed using a semiconductor device simulator (AFORS-HET).[31] It is suggested that conductive materials with large work functions, such as C (5.2 eV) and Au (5.1 eV), are favorable for hole migration from $SrTiO_3$:La,Rh to the conductive material because the Schottky barrier is moderated (Figure 4). Under darkness (Figure 4b), $SrTiO_3$:La,Rh forms Schottky-type barriers at the interfaces with both H_2O and C because of the relative positions of the Fermi levels and the moderate density of holes ($\sim10^{17}$ cm^{-3}) as the majority carrier. On the other hand, $BiVO_4$:Mo does not form appreciable Schottky-type barriers, because the depletion layer width exceeds the dimension of the particle owing to the low electron density ($\sim10^{14}$ cm^{-3}).[33,35] Under steady illumination (Figure 4c), the Schottky-type barriers in $SrTiO_3$:La,Rh are weakened because depleted holes are replenished with photoexcited carriers. Electrons close to the H_2O/$SrTiO_3$:La,Rh interface can migrate to H_2O following the electric field. The energy barrier at the $SrTiO_3$:La,Rh/C interface under illumination is still as large as 0.2 eV and hole migration to the carbon layer by thermal excitation is not energetically favorable. It is considered that
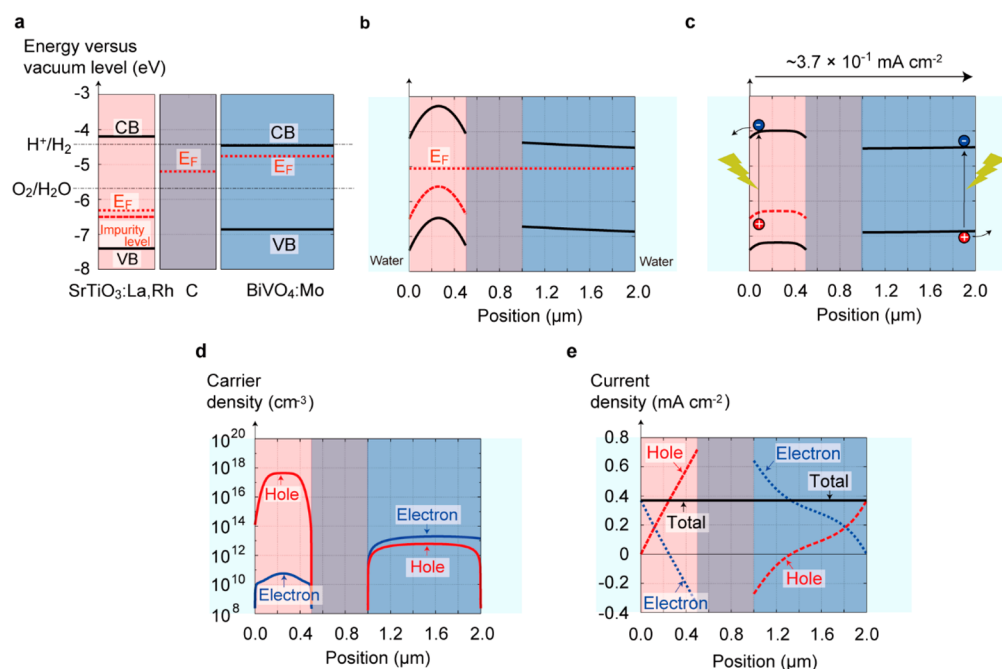
Figure 4. Band diagram and carrier density distribution in SrTiO$_3$:La,Rh/C/BiVO$_4$:Mo sheet. (a−c), Band diagram (a) before contact, (b) under darkness after contact, and (c) under illumination. (d) Carrier density distribution under illumination with a current of 3.7 × 10^{-1} mA cm^{-2}. (e) Current density distribution. The total, electron, and hole current densities are shown by black solid curve, dotted blue, and dashed red curves, respectively. Positive electron and hole current values stand for flow of electrons and holes toward left and right, respectively.

holes accumulate in SrTiO$_3$:La,Rh and migrate to the carbon layer across the Schottky-type barrier by concentration diffusion as shown in Figure 4d. In BiVO$_4$:Mo, on the other hand, electrons and holes can migrate to carbon and H$_2$O, respectively, by diffusion because the band profile is virtually flat and does not have significant energy barriers. In contrast, the use of conductive materials with small work functions, such as Ag (4.3 eV), results in accumulation of photoexcited electrons at the interface (Figure S8 in the Supporting Information). The Schottky-type barrier at the interface of SrTiO$_3$:La,Rh and Ag is steep under darkness because of the small work function of Ag (Figure S8b). Under illumination (Figure S8c), the electron density at the interface with Ag becomes high (∼10^{19} cm^{-3}). Therefore, migration of holes to the Ag layer by concentration diffusion is highly unfavorable. In fact, the current density distribution (Figure S8d) reveals that the hole current density from SrTiO$_3$:La,Rh to Ag is almost zero, suggesting that photogenerated holes in SrTiO$_3$:La,Rh contacting Ag are lost by recombination and do not contribute to the Z-scheme efficiently. The present model would entail uncertainty because accurate parameters of the particulate photocatalysts are missing and defect states at all the interfaces were ignored. Nevertheless, the model can differentiate the behavior of photoexcited carriers in carbon- and silver-based photocatalyst sheets and help to grasp the working mechanism.

Table 1 compares the water-splitting activity of SrTiO$_3$:La,Rh and BiVO$_4$:Mo photocatalysts in the form of a powder suspension, parallel cells, and the present photocatalyst sheet. Although the powder-suspension system decomposed pure water into hydrogen and oxygen stoichiometrically (Entry 1), it exhibited a water-splitting activity that was lower than that for the photocatalyst sheet (Entries 8 and 9) by almost 1 order of magnitude due to the low efficiency of interparticle electron transfer, even at the optimum pH of 3.5 (Entry 2).[46] The gas evolution rate for the powder suspension increased 3-fold when

Table 1. Photocatalytic Activity for Z-Scheme Water Splitting under Visible Light Irradiation Using SrTiO$_3$:La,Rh and BiVO$_4$:Mo in Various Systems[a]

entry	system type	reaction solution	activity/ μmolh^{-1}cm^{-2} H$_2$	O$_2$
1	Powder suspension	Pure water (pH 6.8)	0.4	0.2
2	Powder suspension	Dilute sulfuric acid (pH 3.5)	1.0	0.5
3	Powder suspension	2 mM Iron(III) chloride (pH 2.4)	6.0	2.8
4	Parallel cell	Pure water (pH 6.8)	0.6	0.3
5	Parallel cell	Dilute sulfuric acid (pH 3.5)	1.1	0.6
6	Parallel cell	0.1 M Na$_2$SO$_4$ aq (pH 6.8)	4.5	2.2
7	Parallel cell	0.1 M potassium phosphate aq (pH 6.8)	6.1	2.9
8	Photocatalyst sheet	Pure water (pH 6.8)	8.6	4.4
9	Photocatalyst sheet	Dilute sulfuric acid (pH 3.5)	11	5.5
10	Photocatalyst sheet	2 mM Iron(III) chloride (pH 2.4)	5.5	2.6

[a] All the samples were modified with Ru. Overall water splitting reactions were performed at 288 K and 5 kPa under visible light irradiation (λ > 420 nm).

Fe^{3+}/Fe^{2+} was added as a redox couple to mediate electron transfer[30] between the SrTiO$_3$:La,Rh and BiVO$_4$:Mo (Entry 3). In contrast, the activity of the photocatalyst sheet decreased by two times after adding the redox couple (Entry 10) due to side reactions and shading of the incident light by Fe^{3+}/Fe^{2+}.[30,46] This result further confirms that the photogenerated electrons can transfer from BiVO$_4$:Mo to SrTiO$_3$:La,Rh through the carbon layer.

In parallel cells, the contact layers can be chosen so as to form an ohmic contact between the HEP and OEP. In the present study, a parallel cell was produced using SrTiO$_3$:La,Rh/Au and BiVO$_4$:Mo/Ti photoelectrodes placed side by side. The cell could also steadily produce H$_2$ and O$_2$ in a stoichiometric ratio from pure water (pH 6.8) without an external bias voltage because the photoelectrodes could generate photocathodic and photoanodic currents at the shared electrode potential. However, as shown in Table 1, the poor electrical conductivity of pure water resulted in low activity (Entry 4). The device exhibited higher activity in dilute sulfuric acid (Entry 5) and in a 0.1 M sodium sulfate aqueous solution (Entry 6) because these solutions served as supporting electrolytes with increased conductivity. Note that the pH in the vicinity of the SrTiO$_3$:La,Rh photocathode and BiVO$_4$:Mo photoanode became higher and lower, respectively, during the PEC water-splitting reaction. On the basis of the Nernst equation, the water-electrolysis voltage becomes larger than 1.23 V, and as a result, the water-splitting activity is inevitably reduced. The addition of buffering electrolytes actually increased the water-splitting rate over the parallel cell (Entry 7) because the pH gradient between the two photoelectrodes was suppressed. Nevertheless, adding concentrated buffering reagents could reduce the photocatalytic activity because of specific adsorption of ionic species.[47] In fact, it was shown in our recent work that the water-splitting activity of the SrTiO$_3$:La,Rh/Au/BiVO$_4$:Mo photocatalyst sheet was lowered and gradually decreased during the reaction in an aqueous phosphate buffer.[48] In contrast, the SrTiO$_3$:La,Rh/C/BiVO$_4$:Mo sheet exhibited higher water-splitting rates of 40% and 80% from pure water and dilute sulfuric acid (Entries 8 and 9, respectively) than the powder suspension and parallel cell systems in the best reaction solutions. In addition, the pH of the reaction solutions was unchanged during the reactions. These results indicate that the photocatalyst sheet is free from the H$^+$ and OH$^-$ concentration overpotentials and the IR drops between the hydrogen evolution and oxygen evolution sites that are commonly observed for PEC water splitting. As a consequence, the photocatalyst sheet is directly scalable without any deterioration of its high level of activity.

Effect of Reaction Conditions on Water-Splitting Activity of SrTiO$_3$:La,Rh/C/BiVO$_4$:Mo Sheet. Photocatalytic water-splitting activity generally decreases with increasing background pressure because reverse reactions involving molecular oxygen, such as water formation from the evolved hydrogen and oxygen, and photoreduction of oxygen molecules, readily compete at elevated pressures.[17,49] For instance, the gas evolution rates over a Ru-loaded SrTiO$_3$:La,Rh/Au/BiVO$_4$:Mo photocatalyst sheet[19] and RuO$_2$-loaded (Ga$_{1-x}$Zn$_x$)(N$_{1-x}$O$_x$)[50] were found to decrease to 10% and 40%, respectively, in the presence of 20−30 kPa of argon. Hence, surface modification using Cr$_2$O$_3$[51,52] and amorphous titanium oxide (a-TiO$_2$) layers,[51] which act as molecular sieves to block access by molecular oxygen, are usually necessary in order to suppress the reverse reactions. However, as shown in Figure 5 the Ru-loaded SrTiO$_3$:La,Rh/C/BiVO$_4$:Mo sheet retained 68% of its base performance at 5 kPa at an elevated background pressure of 91 kPa. The water-splitting activity was further enhanced by modification with Cr$_2$O$_3$, although the sensitivity of the water-splitting rate to the background pressure was barely suppressed. Therefore, an a-TiO$_2$ layer was not deposited further onto the carbon-based sample, as it tended to lower the water-splitting activity of
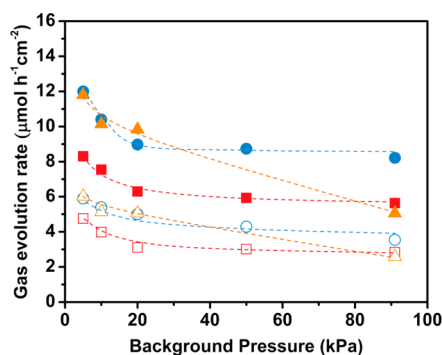

Figure 5. Squares (□), circles (○), and triangles (△) stand for Ru-loaded SrTiO$_3$:La,Rh/C/BiVO$_4$:Mo, Cr$_2$O$_3$/Ru-loaded SrTiO$_3$:La,Rh/C/BiVO$_4$:Mo, and a-TiO$_2$/Cr$_2$O$_3$/Ru-loaded SrTiO$_3$:La,Rh/Au/BiVO$_4$:Mo, respectively. Closed and open symbols represent hydrogen an oxygen, respectively. Photodeposition from RuCl$_3$·3H$_2$O (0.2 μmol), K$_2$CrO$_4$ (0.2 μmol), Ti peroxide (1.3 μmol) and the overall water-splitting reaction were carried out under Xe lamp (300 W) illumination (λ > 420 nm) at 288 K. The area of the photocatalyst sheets was 7.5 cm^2.

photocatalyst sheets at 5 kPa.[19] As a result, the photocatalyst sheet that used the carbon conductor exhibited 64% higher water-splitting activity at ambient pressure than that of the photocatalyst that used the Au conductor and that was optimally modified with Cr$_2$O$_3$ and amorphous TiO$_2$ layers. These observations suggest that the sputtered carbon conductor is less active with regard to reverse reactions than the Au layer used in previous studies.[19] In fact, a Au/Ti electrode had a more positive onset potential for the ORR than a C/Ti electrode, as shown in Figure 6, demonstrating that
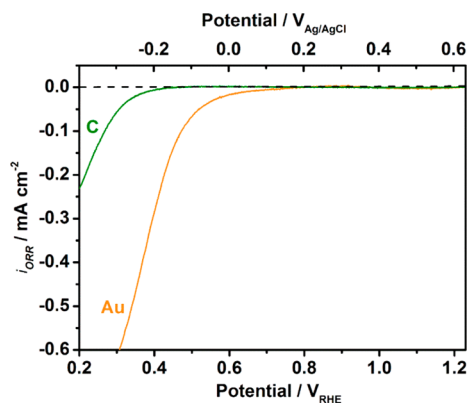

Figure 6. ORR activity of C/Ti (green curve) and Au/Ti (orange curve) electrodes. The electrochemical measurements were performed in a 0.1 M Na$_2$SO$_4$ aqueous electrolyte (pH 6.7) saturated by Ar and O$_2$ atmospheres at 298 K. The i_{ORR} is the difference between the current density measured under O$_2$-saturated and Ar-saturated atmospheres and is regarded as the catalytic activity for the ORR. The potential was cathodically swept at a rate of 10 mV s^{-1}.

oxygen reduction to hydrogen peroxide occurs more readily on gold than on carbon. Accordingly, the photocatalyst sheet with the relatively inert carbon conductor is practical for use at atmospheric pressure. Notably, the photocatalytic activity was still dependent on the background pressure even in the presence of methanol as a sacrificial hole scavenger, where no oxygen was detected in the product gas (Figure S9 in the Supporting Information). Therefore, the drop in the gas

evolution rate with increasing background pressure, particularly below 20 kPa, is attributable to mass transport processes associated with formation and desorption of bubbles from the photocatalyst sheet surface. This is reasonable because the volume of a given amount of gas molecules is inversely proportional to the pressure.

It has been shown in recent studies that PEC and photocatalytic water-splitting reaction rates have a temperature dependence that follows the Arrhenius equation.[19,53,54] During solar-driven photocatalytic water splitting experiments, the temperature of the reactant water has been found to increase to 323−333 K, because a portion of the insolation is used as a heat source.[53,54] Accordingly, we investigated the reaction-temperature dependence of the photocatalytic water-splitting rate over the $SrTiO_3$:La,Rh/C/$BiVO_4$:Mo photocatalyst sheet. Figure 7a
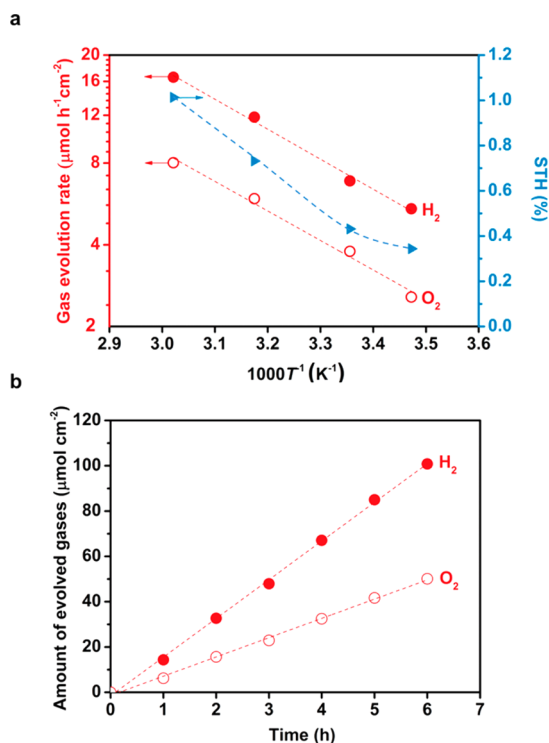
Figure 7. Photocatalytic activity for overall water splitting over Ru-loaded $SrTiO_3$:La,Rh/C/$BiVO_4$:Mo sheet under AM 1.5G simulated sunlight. (a) Temperature dependence of the water-splitting activity and STH at a background pressure of 10 kPa. (b) Time course for overall water splitting. The reaction was carried out at 331 K and 10 kPa.

shows the dependence of the water splitting activity at 10 kPa on the reaction temperature. The water-splitting rate increased by a factor of 3 as the reaction temperature was increased from 288 to 331 K. The apparent activation energy of the overall water-splitting reaction was evaluated to be 21 kJ mol^{-1}, which is close to the value of 18 kJ mol^{-1} estimated for a $SrTiO_3$:La,Rh/Au/$BiVO_4$:Mo sheet.[19] The STH for pure-water (pH 6.8) splitting over a Ru-loaded $SrTiO_3$:La,Rh/C/$BiVO_4$:Mo sample reached 1.0% at 331 K and 10 kPa. In addition, the AQY for the carbon-based photocatalyst sheet was 26% at a wavelength of 419 nm. Notably, the sheet maintained the high water splitting activity for at least 6 h even at the elevated temperature (Figure 7b).

The dependence of the water-splitting rate on the background pressure was further investigated at 331 K as shown in Figure 8 in order to confirm whether the activity could still be
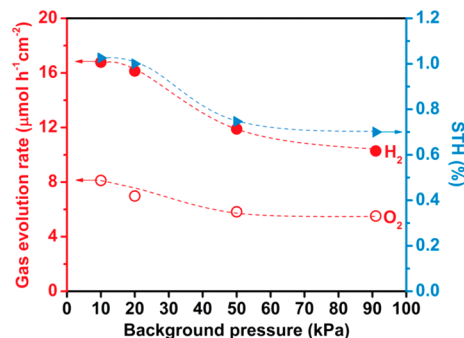
Figure 8. Effect of the background pressure on the photocatalytic water-splitting activity of a Ru-loaded $SrTiO_3$:La,Rh/C/$BiVO_4$:Mo sheet and STH at 331 K under AM 1.5G simulated sunlight.

enhanced by increasing the reaction temperature at elevated background pressures. The STH and AQY values were 0.7% and 19% at 419 nm at near-ambient pressure (91 kPa), which are about 70% of the values at 10 kPa. It is considered from the comparison with Figure 5 that the decrement of the water-splitting activity by increasing the background pressure to the near-ambient pressure was comparable in the temperature range of 288−331 K. Notably, the STH values at 331 K and 10 and 91 kPa were further improved to 1.2% and 1.0%, respectively, by depositing the carbon conductor layer at 373 K and modifying the Ru-loaded $SrTiO_3$:La,Rh/C/$BiVO_4$:Mo sheet with Cr_2O_3 (Figure S10 in the Supporting Information) likely because of a reduction in the contact resistance between the semiconductor particles and the carbon film and the suppression of reverse reactions. At 91 kPa under solar simulator irradiation, gas-bubble formation was observed on the Cr_2O_3/Ru-loaded $SrTiO_3$:La,Rh/C/$BiVO_4$:Mo photocatalyst sheet, as recorded in Movie S1. It should be noted that gas separation processes are needed for the photocatalyst sheet because a mixture of hydrogen and oxygen is produced. Once efficient water splitting is achieved at elevated pressures, gas separation is an issue of chemical engineering balancing a broad range of operations and could be addressed by applying the molecular sieving effect of a microporous membrane, as suggested in our previous work.[19]

■ CONCLUSIONS

Particulate photocatalyst sheets with a high-water-splitting activity at ambient pressure were produced by depositing carbon as an oxygen-tolerant conductor layer. The carbon species deposited were similar to glassy carbon in the properties and characterized with adequate conductivity and large work function. These features were well suited for the use as a conductor film in the present photocatalyst sheet system.

The photocatalyst sheet split pure water without the need for pH control, redox shuttles, supporting electrolytes, buffering reagents, or circulation of the reactants. This was in contrast to the situation for conventional Z-scheme water-splitting and PEC systems, because in the present photocatalyst sheet, the HEP and OEP were in physical proximity to each other on a conducting material, so that hydrogen and oxygen evolution occurred in the vicinity. Photocatalyst sheets exhibited higher performance for overall water splitting than parallel cells

because H^+ and OH^- concentration overpotentials and an *IR* drop between the HEP and OEP were effectively suppressed.

The base performance at 5 kPa of the $SrTiO_3$:La,Rh/C/$BiVO_4$:Mo sheets was largely retained at elevated background pressures because the sputtered carbon conductor was relatively less active with regard to reverse reactions. It achieved a STH of 1.0% during unassisted overall pure-water (pH 6.8) splitting at a temperature of 331 K and a pressure of 91 kPa, which are close to practical operating conditions. This value was 70% higher than the activity of the previously reported $SrTiO_3$:La,Rh/Au/$BiVO_4$:Mo sheets that was optimally modified with Cr_2O_3 and amorphous TiO_2 layers and was the highest among Z-scheme pure water splitting operating at ambient pressure. These sheets are high promising for cost-effective and scalable solar hydrogen production via water splitting. This work enables a deeper understanding of the working mechanism of photocatalysts sheets and offers the important concepts toward development of photocatalytic water splitting systems efficient at ambient pressure.

■ ASSOCIATED CONTENT

Ⓢ Supporting Information

The Supporting Information is available free of charge on the ACS Publications website at DOI: 10.1021/jacs.6b12164.

> Preparation of parallel cells of $SrTiO_3$:La,Rh/Au and $BiVO_4$:Mo/Ti electrodes, photodeposition of cocatalysts, photograph, SEM-EDX images, XRD pattern, photocatalytic activity, and XPS results of $SrTiO_3$:La,Rh/C/$BiVO_4$:Mo sheets, PESA results, band diagram and carrier density distribution in $SrTiO_3$:La,Rh/Ag/$BiVO_4$:Mo sheet, and material parameters used for the band diagram calculation (PDF)
> Movie S1 (AVI)

■ AUTHOR INFORMATION

Corresponding Author

*domen@chemsys.t.u-tokyo.ac.jp

ORCID Ⓞ

Takashi Hisatomi: 0000-0002-5009-2383

Kazunari Domen: 0000-0001-7995-4832

Notes

The authors declare no competing financial interest.

■ ACKNOWLEDGMENTS

■ REFERENCES

(1) Armstrong, R. C.; Wolfram, C.; de Jong, K. P.; Gross, R.; Lewis, N. S.; Boardman, B.; Ragauskas, A. J.; Ehrhardt-Martinez, K.; Crabtree, G.; Ramana, M. V. *Nat. Energy* **2016**, *1*, 15020−15027.

(2) Lewis, N. S. *Science* **2016**, *351*, aad1920.

(3) McKone, J. R.; Lewis, N. S.; Gray, H. B. *Chem. Mater.* **2014**, *26*, 407−414.

(4) Walter, M. G.; Warren, E. L.; McKone, J. R.; Boettcher, S. W.; Mi, Q.; Santori, E. A.; Lewis, N. S. *Chem. Rev.* **2010**, *110*, 6446−6473.

(5) Pinaud, B. A.; Benck, J. D.; Seitz, L. C.; Forman, A. J.; Chen, Z.; Deutsch, T. G.; James, B. D.; Baum, K. N.; Baum, G. N.; Ardo, S. *Energy Environ. Sci.* **2013**, *6*, 1983−2002.

(6) Fujishima, A. *Nature* **1972**, *238*, 37−38.

(7) Abdi, F. F.; Han, L.; Smets, A. H. M.; Zeman, M.; Dam, B.; van de Krol, R. *Nat. Commun.* **2013**, *4*, 2195.

(8) Brillet, J.; Yum, J.-H.; Cornuz, M.; Hisatomi, T.; Solarska, R.; Augustynski, J.; Graetzel, M.; Sivula, K. *Nat. Photonics* **2012**, *6*, 824−828.

(9) Chen, Y.-S.; Manser, J. S.; Kamat, P. V. *J. Am. Chem. Soc.* **2015**, *137*, 974−981.

(10) Khaselev, O.; Turner, J. A. *Science* **1998**, *280*, 425−427.

(11) Ager, J. W.; Shaner, M. R.; Walczak, K. A.; Sharp, I. D.; Ardo, S. *Energy Environ. Sci.* **2015**, *8*, 2811−2824.

(12) Osterloh, F. E. *J. Phys. Chem. Lett.* **2014**, *5*, 2510−2511.

(13) Gratzel, M. *Nature* **2001**, *414*, 338−344.

(14) Shaner, M. R.; Atwater, H. A.; Lewis, N. S.; McFarland, E. W. *Energy Environ. Sci.* **2016**, *9*, 2354−2371.

(15) Kudo, A.; Miseki, Y. *Chem. Soc. Rev.* **2009**, *38*, 253−278.

(16) Yuan, Y.-P.; Ruan, L.-W.; Barber, J.; Joachim Loo, S. C.; Xue, C. *Energy Environ. Sci.* **2014**, *7*, 3934−3951.

(17) Hisatomi, T.; Kubota, J.; Domen, K. *Chem. Soc. Rev.* **2014**, *43*, 7520−7535.

(18) Maeda, K. *ACS Catal.* **2013**, *3*, 1486−1503.

(19) Wang, Q.; Hisatomi, T.; Jia, Q.; Tokudome, H.; Zhong, M.; Wang, C.; Pan, Z.; Takata, T.; Nakabayashi, M.; Shibata, N.; Li, Y.; Sharp, I. D.; Kudo, A.; Yamada, T.; Domen, K. *Nat. Mater.* **2016**, *15*, 611−615.

(20) Kato, H.; Sasaki, Y.; Shirakura, N.; Kudo, A. *J. Mater. Chem. A* **2013**, *1*, 12327−12333.

(21) Wang, Q.; Li, Y.; Hisatomi, T.; Nakabayashi, M.; Shibata, N.; Kubota, J.; Domen, K. *J. Catal.* **2015**, *328*, 308−315.

(22) Shiraishi, M.; Ata, M. *Carbon* **2001**, *39*, 1913−1917.

(23) Michaelson, B. H. *J. Appl. Phys.* **1977**, *48*, 4729−4733.

(24) Uosaki, K.; Elumalai, G.; Noguchi, H.; Masuda, T.; Lyalin, A.; Nakayama, A.; Taketsugu, T. *J. Am. Chem. Soc.* **2014**, *136*, 6542−6545.

(25) Lu, Y.-C.; Gasteiger, H. A.; Shao-Horn, Y. *J. Am. Chem. Soc.* **2011**, *133*, 19048−19051.

(26) Bezerra, C. W. B.; Zhang, L.; Liu, H.; Lee, K.; Marques, A. L. B.; Marques, E. P.; Wang, H.; Zhang, J. *J. Power Sources* **2007**, *173*, 891−908.

(27) Wang, Q.; Hisatomi, T.; Ma, S. S. K.; Li, Y.; Domen, K. *Chem. Mater.* **2014**, *26*, 4144−4150.

(28) Kudo, A.; Omori, K.; Kato, H. *J. Am. Chem. Soc.* **1999**, *121*, 11459−11467.

(29) Minegishi, T.; Nishimura, N.; Kubota, J.; Domen, K. *Chem. Sci.* **2013**, *4*, 1120−1124.

(30) Sasaki, Y.; Iwase, A.; Kato, H.; Kudo, A. *J. Catal.* **2008**, *259*, 133−137.

(31) Varache, R.; Leendertz, C.; Gueunier-Farret, M. E.; Haschke, J.; Muñoz, D.; Korte, L. *Sol. Energy Mater. Sol. Cells* **2015**, *141*, 14−23.

(32) Kawasaki, S.; Takahashi, R.; Akagi, K.; Yoshinobu, J.; Komori, F.; Horiba, K.; Kumigashira, H.; Iwashina, K.; Kudo, A.; Lippmaa, M. *J. Phys. Chem. C* **2014**, *118*, 20222−20228.

(33) Rettie, A. J.; Lee, H. C.; Marshall, L. G.; Lin, J.-F.; Capan, C.; Lindemuth, J.; McCloy, J. S.; Zhou, J.; Bard, A. J.; Mullins, C. B. *J. Am. Chem. Soc.* **2013**, *135*, 11389−11396.

(34) Zhao, Z.; Li, Z.; Zou, Z. *Phys. Chem. Chem. Phys.* **2011**, *13*, 4746−4753.

(35) Payne, D. J.; Robinson, M. D. M.; Egdell, R. G.; Walsh, A.; McNulty, J.; Smith, K. E.; Piper, L. F. *J. Appl. Phys. Lett.* **2011**, *98*, 212110.

(36) Hong, S. J.; Lee, S.; Jang, J. S.; Lee, J. S. *Energy Environ. Sci.* **2011**, *4*, 1781−1787.

(37) Konta, R.; Ishii, T.; Kato, H.; Kudo, A. *J. Phys. Chem. B* **2004**, *108*, 8992−8995.

(38) Valant, M.; Suvorov, D. *J. Am. Ceram. Soc.* **2000**, *83*, 2721−2729.

(39) Frederikse, H.; Thurber, W.; Hosler, W. *Phys. Rev.* **1964**, *134*, A442−A445.

(40) Weaver, H. *J. Phys. Chem. Solids* **1959**, *11*, 274−277.

(41) Li, M.; Bo, X.; Zhang, Y.; Han, C.; Nsabimana, A.; Guo, L. *J. Mater. Chem. A* **2014**, *2*, 11672−11682.

(42) Cuomo, J. J.; Pappas, D. L.; Bruley, J.; Doyle, J. P.; Saenger, K. L. *J. Appl. Phys.* **1991**, *70*, 1706−1711.

(43) Dwivedi, N.; Yeo, R. J.; Satyanarayana, N.; Kundu, S.; Tripathy, S.; Bhatia, C. S. *Sci. Rep.* **2015**, *5*, 7772.

(44) Ferrari, A. C.; Robertson, J. *Phys. Rev. B: Condens. Matter Mater. Phys.* **2000**, *61*, 14095−14107.

(45) Schwan, J.; Ulrich, S.; Batori, V.; Ehrhardt, H.; Silva, S. *J. Appl. Phys.* **1996**, *80*, 440−447.

(46) Sasaki, Y.; Nemoto, H.; Saito, K.; Kudo, A. *J. Phys. Chem. C* **2009**, *113*, 17536−17542.

(47) Maeda, K.; Masuda, H.; Domen, K. *Catal. Today* **2009**, *147*, 173−178.

(48) Wang, Q.; Hisatomi, T.; Katayama, M.; Takata, T.; Minegishi, T.; Kudo, A.; Yamada, T.; Domen, K. *Faraday Discuss.* **2017**, DOI: 10.1039/C6FD00184J.

(49) Takata, T.; Pan, C.; Domen, K. *Sci. Technol. Adv. Mater.* **2015**, *16*, 033506.

(50) Maeda, K.; Teramura, K.; Masuda, H.; Takata, T.; Saito, N.; Inoue, Y.; Domen, K. *J. Phys. Chem. B* **2006**, *110*, 13107−13112.

(51) Takata, T.; Pan, C.; Nakabayashi, M.; Shibata, N.; Domen, K. *J. Am. Chem. Soc.* **2015**, *137*, 9627−9634.

(52) Maeda, K.; Teramura, K.; Lu, D.; Saito, N.; Inoue, Y.; Domen, K. *Angew. Chem., Int. Ed.* **2006**, *45*, 7806−7809.

(53) Pihosh, Y.; Turkevych, I.; Mawatari, K.; Uemura, J.; Kazoe, Y.; Kosar, S.; Makita, K.; Sugaya, T.; Matsui, T.; Fujita, D.; Tosa, M.; Kondo, M.; Kitamori, T. *Sci. Rep.* **2015**, *5*, 11141.

(54) Licht, S. *Electrochem. Commun.* **2002**, *4*, 790−795.